SCIENCE CHINA
Technological Sciences

• Article •

March 2020 Vol. 63 No. 3: 496–505
https://doi.org/10.1007/s11431-018-9524-2

A two degree of freedom stable quasi-zero stiffness prototype and its applications in aseismic engineering

ZHU GuangNan[1], LIU JiYe[1], CAO QingJie[1*], CHENG YongFeng[2], LU ZhiCheng[2] & ZHU ZhuBing[2]

[1]*School of Astronautics, Harbin Institute of Technology, Harbin 150001, China;*
[2]*China Electric Power Research Institute, Beijing 100055, China*

Received December 19, 2018; accepted May 10, 2019; published online January 10, 2020

In this paper, an archetypal aseismic system is proposed with 2-degree of freedom based on a smooth and discontinuous (SD) oscillator to avoid the failure of electric power system under the complex excitation of seismic waves. This model comprises two vibration isolation units for the orthogonal horizontal directions, and each of them admits the stable quasi-zero stiffness (SQZS) with a pair of inclined linear elastic springs. The equation of motion is formulated by using Lagrange equation, and the SQZS condition is obtained by optimizing the parameters of the system. The analysis shows that the system behaves a remarkable vibration isolation performance with low resonant frequency and a large stroke of SQZS interval. The experimental investigations are carried out to show a high sonsistency with the theoretical results, which demonstrates the improvement of aseismic behavior of the proposed model under the seismic wave.

SD oscillator, two-DOF vibration isolation, stable quasi-zero stiffness, low-frequency vibration isolation, aseismic experiment

Citation: Zhu G N, Liu J Y, Cao Q J, et al. A two degree of freedom stable quasi-zero stiffness prototype and its applications in aseismic engineering. Sci China Tech Sci, 2020, 63: 496–505, https://doi.org/10.1007/s11431-018-9524-2

1 Introduction

This work is motivated by the increasing concern for the seismic hazard resulted from the low frequency seismic waves in horizontal directions to electric power system [1–5]. Rubber bearings are widely used in most of the aseismic construction for high voltage transformers based on the traditional isolation theory which has a weaker vibration isolation performance for low frequency band [6–11]. However, huge kinetic energy stored in seismic waves is at the low frequency brand [12], taken a power spectral density (PSD) curve of a real earthquake ground acceleration record for example, as shown in the figure in Sect. 3, most of the energy of the seismic wave is concentrated between 0.1 and 10 Hz. There are 137 transformer substations over 110 kV are destructed resulting in 181 transmission lines shutdown during a magnitude 8.0 earthquake occurred in Wenchuan, Sichuan Province, China in May 12, 2008 [13–16]. The same disaster happened in the magnitude 8.0 earthquake in Ya'an City of Sichuan Province in April 20, 2013, there are 34 transformer substations and 626 transformation equipments shutdown [17–19].

Recent years, several types of isolators with stable quasi-zero-stiffness (SQZS) characteristics have been studied. Alabuzhev et al. [20] designed a kind of vibration isolator with positive and negative stiffness elastic elements in parallel. Zhang et al. [21] proposed an isolator to provide the precision instruments at the frequency lower than 0.5Hz, which consisted by an elastic component and Euler column. Some designs can provide very low stiffness by using the buckled Euler column as the negative stiffness component [22–24], and some others utilized the pinched loop to achieve a low frequency isolator [25, 26]. Zhou and Liu [27] presented a

*Corresponding author (email: qingjiecao@hotmail.com)

high static and low dynamic stiffness devices with a regulating system. Robertson et al. [28] exploited a kind of SQZS isolator with fully magnetic springs. Xu et al. [29, 30] proposed abundant research findings for geometric nonlinear vibration isolatior with the SQZS characteristic, such as camroller-spring and magnetic spring mechanism. Attention has been made on low frequency vibration isolation with SQZS [31–33] based upon a named smooth and discontinuous (SD) oscillator [34] proposed by Cao et al., consisting of a lumped mass and a pair of elastic springs. Several studies on its dynamics, including negative stiffness characteristics [35], have been presented and is deeply developed recently [36–41]. It has been proved that this kind of system can improve the isolation performance significantly in a low frequency brand [42–46].

The motivation of this paper is to propose an archetypal vibration isolator with SQZS in multiple directions based on the SD oscillator to protect the structure failure from the complex earthquake waves horizontally. Another motivation is to understand the failure mechanism of the system, by evaluating the response of the system under the harmonic and the recorded earthquake wave excitations, respectively. Finally, this paper is to investigate the theoretical results experimentally.

2 SQZS analysis

Consider a vibration isolation system based upon the SD oscillator, as shown in Figure 1, which comprises a lumped mass, m, linked by a pair of linear elastic springs, with the stiffness k, the assembly length l and the equilibrium length L. A damper with the damping coefficient of C is installed along the direction in which the displacement of the mass is limited. Define X is the displacement of the lumped mass, and Y is the displacement of the basement, further, $Z = X - Y$ is the displacement of lumped mass relative to the basement.

Assuming that the mass produces relative displacement of Z, the length of a each oblique spring can be expressed as

$$L_s = \sqrt{Z^2 + l^2}, \tag{1}$$

based upon the geometric relation. The elastic force produced by each spring can be obtained as

$$F_s = k\left(L_s - L\right). \tag{2}$$

Thus, the restoring force of system along the direction Z is

$$F\left(Z\right) = 2F_s \frac{Z}{L_s}. \tag{3}$$

The equation of motion can be written as

$$mX'' + CX' + 2k\left(1 - \frac{L}{\sqrt{Z^2 + l^2}}\right)Z = 0, \tag{4}$$

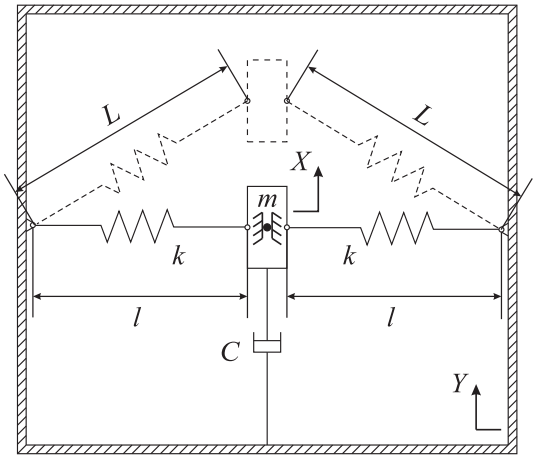

Figure 1 Vibration isolation unit for a single direction.

where X' and X'' represent the first and second order derivative of the displacement X to the time t, respectively, and the following are the same. The equivalent stiffness of the system can be obtained, written as

$$K\left(Z\right) = \frac{\partial F\left(Z\right)}{\partial Z} = 2k\left(1 - \frac{l^2 L}{\left(Z^2 + l^2\right)^{\frac{3}{2}}}\right), \tag{5}$$

then the SQZS condition can be obtained by letting $K\left(0\right) = 0$, written as

$$L = l. \tag{6}$$

Substituting eq. (6) into eq. (4), the equation of motion of the SQZS vibration isolation system is shown as following:

$$mX'' + CX' + 2k\left(1 - \frac{l}{\sqrt{Z^2 + l^2}}\right)Z = 0. \tag{7}$$

Considering the condition of the static basement, that is $Y = 0$. Then the dimensionless dynamic equation will be transformed into the following form:

$$z'' + \zeta z' + \omega_0^2\left(1 - \frac{1}{\sqrt{z^2 + 1^2}}\right)z = 0, \tag{8}$$

where $z = Z/l$, $\zeta = C/\left(m\omega_0\right)$, $\omega_0^2 = 2k/m$. The curves of the dimensionless restoring force and equivalent stiffness with different ω_0 are shown in Figure 2. Combined with actual working conditions, let ratio of the stiffness and the mass $\omega_0^2 = 25$, 30, and 35, we can notice that the restoring force is very close to zero in the case of a small displacement emerged, from Figure 2(a). And the Figure 2(b) shows that the equivalent stiffness is always greater than or equals

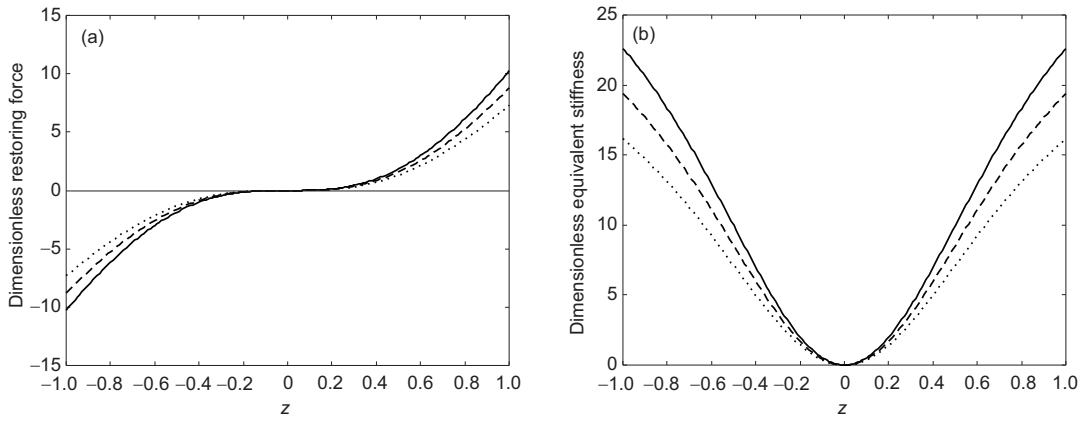

Figure 2 Dimensionless restoring force and equivalent stiffness curves with the parameter $\omega_0 = \sqrt{25}$, $\sqrt{30}$, and $\sqrt{35}$, plotted by dotted, dashed, and solid lines, respectively. (a) The restoring force; (b) the equivalent stiffness.

to zero, and only when the lump mass at the equilibrium position of the system, the equivalent stiffness equals to zero. This is the most important statics characteristic of SQZS system. That means the system has a stable restoring force in the whole range, and the variance ratio is small enough within a certain range. In other words, this kind of system reduces the natural frequency to the minimum under the premise of ensuring stability, so that it can improves the performance of low frequency vibration isolation.

3 Isolation analysis

Considering the forced nonconservative SQZS system with the base displacement $Y = B\cos\Omega t$ in eq. (4), the equation of motion can be written as

$$mZ'' + CZ' + 2k\left(1 - \frac{l}{\sqrt{Z^2 + l^2}}\right)Z = mB\Omega^2\cos\Omega t. \tag{9}$$

The dimensionless equation can be written as the following by letting $z = Z/l$, $\omega_0^2 = 2k/m$, $\tau = \omega_0 t$, $\omega = \Omega/\omega_0$, $\zeta = C/(m\omega_0)$, and $b = B/l$.

$$\ddot{z} + \zeta\dot{z} + \left(1 - \frac{1}{\sqrt{z^2+1}}\right)z = b\omega^2\cos\omega\tau, \tag{10}$$

where $\dot{z}$ and $\ddot{z}$ represent the first and second derivatives of the dimensionless displacement z to the dimensionless time τ, respectively, and the following are the same. Taylor expand the unjustifiable term $\left(1 - \frac{1}{\sqrt{z^2+1}}\right)z$ at $z = 0$ to avoid the introduction of elliptic integral, then eq. (10) reads

$$\ddot{z} + \zeta\dot{z} + \frac{1}{2}z^3 = b\omega^2\cos\omega\tau. \tag{11}$$

Assuming the solution of the system (11) is periodic, using the averaging method and substituting

$$\begin{cases} z = a\cos(\omega\tau - \phi), \\ \dot{z} = -a\omega\sin(\omega\tau - \phi), \end{cases} \tag{12}$$

into eq. (11), it can yield the equations of slowly varying amplitude and phase as that

$$\begin{cases} \dot{a} = -\dfrac{1}{\omega}P(a,\phi)\sin(\omega\tau - \phi), \\ \dot{\phi} = -\dfrac{1}{a\omega}P(a,\phi)\cos(\omega\tau - \phi), \end{cases} \tag{13}$$

in which

$$P(a,\phi) = b\omega^2\cos\omega\tau + \zeta a\omega\sin(\omega\tau - \phi) + a\omega^2\cos(\omega\tau - \phi) - \frac{1}{2}a^3\cos^3(\omega\tau - \phi). \tag{14}$$

By averaging $\psi = \omega\tau - \phi$ for eq. (13) over a period from 0 to 2π, the averaging equation with respect to a and ϕ is written as

$$\begin{cases} \dot{a} = \dfrac{1}{2}(-a\zeta + b\omega\sin\phi), \\ \dot{\phi} = \dfrac{1}{2}\left(\dfrac{3a^2}{8\omega} - \omega - \dfrac{b\omega}{a}\cos\phi\right). \end{cases} \tag{15}$$

Let $\dot{a} = 0$, $\dot{\phi} = 0$ that derive singular point (a_s, ϕ_s) that corresponds to the periodic solution of steady state of the eq. (11), which satisfies

$$\begin{cases} \sin\phi = \dfrac{a\zeta}{b\omega}, \\ \cos\phi = \dfrac{a\left(3a^2 - 8\omega^2\right)}{8b\omega^2}. \end{cases} \tag{16}$$

Then the relationship of the amplitude of relative displacement a and frequency ω is derived by employing the averag-

ing technique as the following:

$$(b\omega)^2 - (a\zeta)^2 = \left(\frac{3a^3}{8\omega} - a\omega\right)^2. \tag{17}$$

It is clear that the dimensionless absolute displacement is in the following form:

$$\begin{cases} x = c\cos(\omega\tau + \theta) = z + y = a\cos(\omega\tau - \phi) + b\cos\omega\tau \\ \quad = \sqrt{a^2 + b^2 + 2ab\cos\phi}\cos(\omega\tau + \theta), \\ \cot\theta = -\dfrac{a\cos\phi + b}{a\sin\phi}, \end{cases} \tag{18}$$

from which the relationship between amplitude of absolute displacement c and relative displacement a is shown as following by eliminating the phase angle $\cos\phi$ using eq. (16):

$$c^2 = -a^2 + b^2 + \frac{3a^4}{4\omega^2}. \tag{19}$$

The equation of the amplitude of absolute displacement c and frequency ω can be obtained, by substituting eq. (19) into eq. (17):

$$3b^2 - 3c^2 - \omega^2 + \left(\omega - \frac{6\left(b^2 + 3c^2\right)\omega}{-3b^2 + 3c^2 + 4\left(4\zeta^2 + \omega^2\right)}\right)^2 = 0. \tag{20}$$

Define

$$T_a = \frac{\ddot{x}_{\max}}{\ddot{y}_{\max}} = \frac{\sqrt{\left(\frac{3}{8}a^3\right)^2 + (\zeta a\omega)^2}}{\omega^2 b}, \tag{21}$$

and

$$T_d = \frac{x_{\max}}{y_{\max}} = \frac{c}{b} \tag{22}$$

are the transmissibility of the acceleration and absolute displacement of the system, respectively. The acceleration transmissibility relationship can be obtained by simultaneous eqs. (17) and (21), and the absolute displacement transmissibility relationship can be obtained by simultaneous eqs. (20) and (22) as the following:

$$\frac{27b^4\left(1 + 3T_a^2\right)^3\omega^2}{\left(3b^2\left(-1 + T_a^2\right) + 4\left(4\zeta^2 + \omega^2\right)\right)^3} + \frac{32\zeta^2\left(1 + 3T_a^2\right)}{3b^2\left(-1 + T_a^2\right) + 4\left(4\zeta^2 + \omega^2\right)} = 8T_a^2, \tag{23}$$

and

$$3b^2 - 3b^2T_d^2 - \omega^2 + \left(\omega - \frac{6b^2\left(1 + 3T_d^2\right)\omega}{3b^2\left(-1 + T_d^2\right) + 4\left(4\zeta^2 + \omega^2\right)}\right)^2 = 0, \tag{24}$$

respectively.

Figure 3(a) and (b) exhibits the acceleration transmissibility and absolute displacement transmissibility curves for eqs. (23) and (24), respectively, with the amplitude $b = 0.5$ and the different damping ratio, $\zeta = 0.31$, 0.32 and 0.33, for dotted, dashed, and solid lines, separately. It is interesting that there is an almost fixed point at the frequency ω^* for both Figure 3(a) and (b) and the transmissibility will decrease and increase as the damping ratio increase for $\omega < \omega^*$ and $\omega > \omega^*$, respectively, along the dashed arrow, as shown in both Figure 3(a) and (b). This implies that even the resonance can be restrained by increasing the damping, the increasing damping will result in the isolation performance sacrificed for the high frequency band. It is found from Figure 3(b) that the jumping phenomenon occurs for lower damping ratio, the transmissibility curve will increase along the arrow 1 as the frequency increase from 0 and then drop to the lower branch

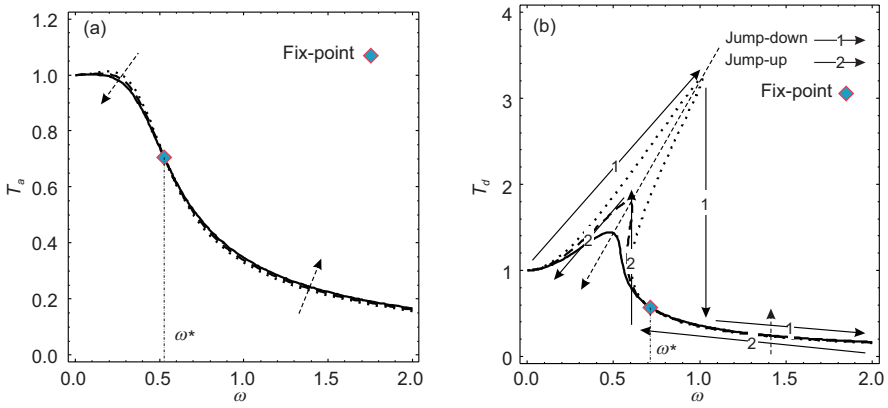

Figure 3 (Color online) The acceleration transmissibility and absolute displacement transmissibility curves with the damping ratio $\zeta = 0.31$, 0.32, and 0.33, plotted by dotted, dashed, and solid lines, respectively. (a) The acceleration transmissibility; (b) the absolute displacement transmissibility.

suddenly and decrease. Correspondingly, the transmissibility will increase along the arrow 2 as the frequency decreases and then jumps to the higher branch immediately and decrease, as shown in Figure 3(b), which implies the jumping phenomenon can be eliminated by choosing proper damping.

The system may still exhibit many other types of solutions besides the principal resonance solution, based on the nonlinear characteristic, such as the ultraharmonic, subharmonic, and chaotic solutions. However, this paper mainly focuses on the isolation performance of the system for seismic waves, so the other types of solutions will not be analyzed or discussed in detail.

Considering a real earthquake ground motion record provided by China Electric Power Research Institute, whose spectrum is shown in Figure 4. The maximum acceleration of $0.4g$ at the duration of 43.98 s, as shown in Figure 4(a). It is found that from Figure 4(b) the most of the energy is concentrated between 0.1 and 10 Hz with a peak at about 1 Hz. Combining with the actual design requirement of vibration isolator, we assuming the mass of the loading and the isolator are $m = 200$ kg and $M = 150$ kg, respectively, and the width of the prototype $l = 0.2$ m, in the following calculations.

Figure 3(a) and (b) shows that the absolute displacement transmissibility is more sensitive to the damping ratio ζ than the acceleration transmissibility, and the absolute displacement transmissibility resonance phenomenon in the low frequency region is more obvious than the acceleration transmissibility. In order to narrow the range of optimal system parameters C and k, the following restrictions are given based on the absolute displacement transmissibility (24).

(1) Suppressing the jumping phenomenon of the transmissibility curve to avoid the uncertainty caused by the initial value of the system response. That means the transmissibility of the system has and only has a single solution at any excitation frequency ω. The relationship between frequency ω and transmissibility T_d is expressed as an explicit function as follows:

$$\omega^2 = \omega_2\left(T_d^2\right) = \frac{1}{8T_d^2}\left(\zeta^2\left(4 - 20T_d^2\right) + 3b^2T_d^2\left(3 + T_d^2\right) \pm \sqrt{\left(1 + 3T_d^2\right)^2\left(16\zeta^4 + 9b^4T_d^2 - 24b^2\zeta^2T_d^2\right)}\right) \tag{25}$$

based on eq. (24). Let the number of roots of the equation, shown as following:

$$\frac{\mathrm{d}\left(\omega^2\right)}{\mathrm{d}\left(T_d^2\right)} = 0, \tag{26}$$

be no more than 1. Solving the eq. (26), the roots can be obtained as following:

$$T_d^2 = \frac{45b^4 - 144b^2\zeta^2 \pm \sqrt{3}\sqrt{243b^8 - 3168b^6\zeta^2 + 13056b^4\zeta^4 - 16384b^2\zeta^6}}{2\left(36b^4 - 96b^2\zeta^2\right)}. \tag{27}$$

When the present formula, written as

$$243b^8 - 3168b^6\zeta^2 + 13056b^4\zeta^4 - 16384b^2\zeta^6 \leqslant 0, \tag{28}$$

holds, the restriction can be satisfied.

(2) The initial isolation frequency ω^* is lower than 1 Hz, to ensure that the isolator can effectively isolate most of the energy of seismic waves. Let $243b^8 - 3168b^6\zeta^2 + 13056b^4\zeta^4 - 16384b^2\zeta^6 = 0$, and the transmissibility satisfies

$$T_d^2 = \frac{45b^4 - 144b^2\zeta^2}{2\left(36b^4 - 96b^2\zeta^2\right)}. \tag{29}$$

The restriction can be satisfied when the following relationship, shown as

$$\omega^{*2} = -352\zeta^2 - \frac{2\sqrt{2}\left(3b^2 - 8\zeta^2\right)\sqrt{\frac{\left(69b^2 - 208\zeta^2\right)^2\left(45b^4 - 144b^2\zeta^2 + 128\zeta^4\right)}{\left(3b^2 - 8\zeta^2\right)^2}}}{5b^2 - 16\zeta^2} + b^2\left(261 + \zeta^2\left(\frac{128}{5b^2 - 16\zeta^2} + \frac{72}{-3b^2 + 8\zeta^2}\right)\right) \leqslant \frac{768\pi^2}{\omega_0^2} \tag{30}$$

is established by substituting eq. (29) into eq. (25).

(3) The transmissibility response is no more than 0.6 at the external excitation frequency equals to 1 Hz. It can be proved that the transfer rate is a subtraction function of frequency,

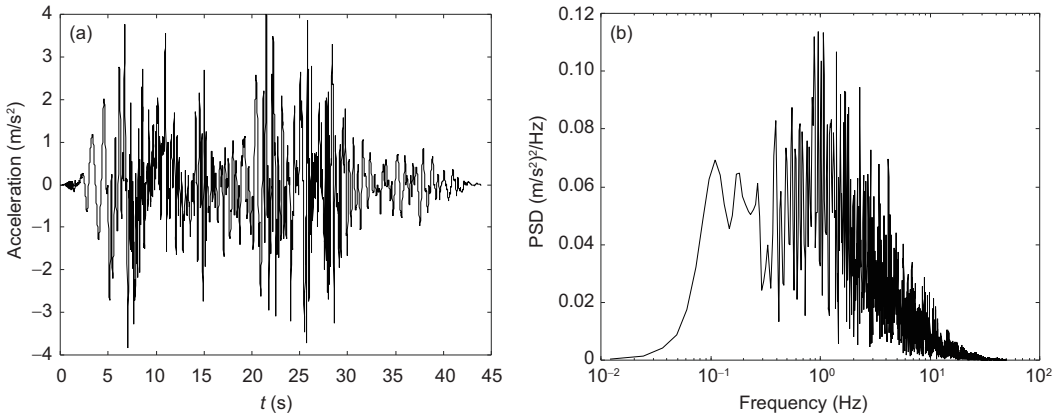

Figure 4 The time domain and frequency domain spectrum of a real earthquake ground acceleration record. (a) The time domain spectrum; (b) the power spectral density (PSD) curve of the spectrum.

based upon the conclusion of the restriction 1 that there is no jumping phenomenon and the restriction 2 that the initial isolation frequency is lower than 1 Hz. Thus, this restriction can be reinterpreted as

$$\omega^{*2} \leqslant \omega_2 \left(0.6^2\right)_{\max} \leqslant \frac{4\pi^2}{\omega_0^2}. \tag{31}$$

The intersection of inequalities eq. (28), (30) and (31) is solved according to the actual engineering design requirements, where $\omega_0 = \sqrt{k/m}$ and $b = B/l = a/\left(4\pi^2 ml\right)$. The design range of the optimal parameters C and k is limited as following:

$$\begin{cases} \zeta \in [0.25, 0.6], \\ k \in [2500\ \text{N/m}, 3500\ \text{N/m}]. \end{cases} \tag{32}$$

4 Determination of parameters

In this section, the vibration isolation performance of the system under the seismic acceleration record is investigated and the physical parameters are optimized.

The equation of motion under the seismic acceleration excitation is established as the following:

$$mZ'' + CZ' + 2k\left(1 - \frac{l}{\sqrt{Z^2 + l^2}}\right)Z = MS(t), \tag{33}$$

where M is the mass of the isolator, and $S(t)$ is the seismic acceleration record which is shown in Figure 4.

The optimization of parameters k and C in eq. (33) are carried out numerically using Runge-Kutta Method to match the minimum of acceleration peaks within the limit of the relative displacement peaks less than $l_0 < l$ to ensure the safety of the isolator. Figure 5(a) and (b) is the acceleration peak surface and the relative displacement peak surface, respectively, over the range obtained by eq. (32). It is found from the figures that the optimized damping is $\zeta \approx 0.39$, at which both the acceleration and the relative displacement peak reaches the minimum value, respectively. In the same way, the stiffness can also be optimized at $k = 3000$ N/m by considering the monotone increasing of the acceleration and the decreasing of the relative displacement with respect to stiffness k to get the minimum acceleration, that is, the maximum relative displacement which is taken as $l_0 = 0.15$ m less than $l = 0.2$ m.

Figure 6(a) and (b) shows the time domain and the frequency domain spectrum of the acceleration response, respectively, with the optimized parameters $C = 302.093$ Ns/m and $k = 3000$ N/m, the seismic spectrum marked black, the response spectrum of linear system marked green, and the response spectrum of SQZS system marked red. It can be seen that the linear system has certain vibration attenuation ability, but there is still a phenomenon of vibration amplification, such as 3.32 to 5.95 s, 19.31 to 21.37 s, and 29.71 to 45 s, from Figure 6(a). Correspondingly, this kind of system has the initial vibration isolation frequency at $f_l^* \approx 1.221$ Hz. It can be seen that from Figure 6(a) the acceleration of nonlinear system has been attenuated by 47.775% with the maximum value at 0.209 g. It can also be found that from Figure 6(b) the initial vibration isolation frequency $f_n^* \approx 0.525$ Hz. The results present here show the good aseismic performance than the traditional linear vibration isolation system for low frequency band.

5 Experimental analysis

The CAD model of the proposed vibration isolator presented in Sect. 2 is established to help design of the isolator, which consists of two vibration isolation units, Y direction (unit Y) and X direction (unit X), as shown in Figure 7. Figure 7(a) presents the structural of unit X, the blue indicates the guiding (X direction) slide-rails fixed on the base, the red is the

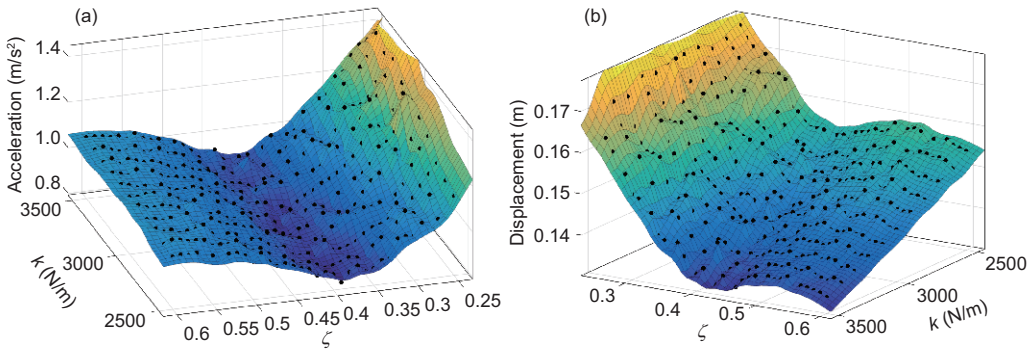

Figure 5 The acceleration and the relative displacement responses under the seismic acceleration record, with the different stiffness and damping ratio. (a) The acceleration response; (b) the relative displacement response.

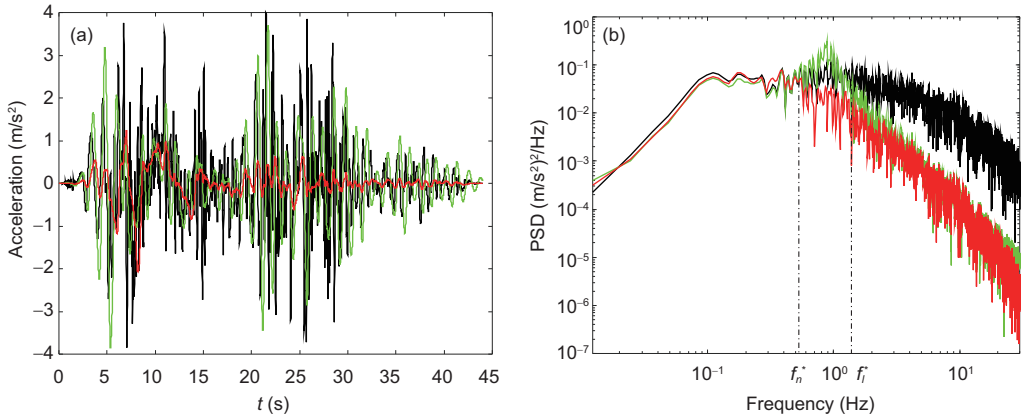

Figure 6 The time domain and frequency domain spectrum of acceleration response with the optimal parameter configuration. (a) The time domain spectrum; (b) the frequency domain spectrum.

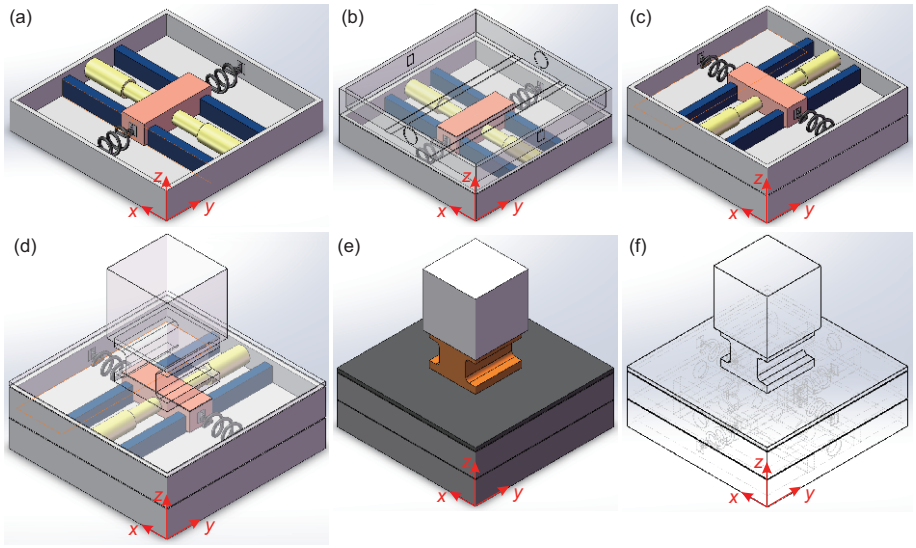

Figure 7 The CAD model of vibration isolator.

slider along the slide-rails, and a pair of springs (shown in black structure) and dampers (shown in yellow structure) are arranged along the directions perpendicular and parallel to the slide-rails connecting the base and the slider, respectively. The Figure 7(b) and (c) shows the details of the unit *Y* which has the same internal structure with unit *X*, and the base of the unit *Y* is fixed on the slider of unit *X* to ensure the two slide-rails of unit *X* and unit *Y* are orthogonal to each other.

The platform and the loading (shown as the block in Figure 7(e) and (f) to substitute the protected power equipment) is connected with the slider of the unit Y, as shown in Figure 7(d). The Figure 7(e) and (f) provides the panorama and the scenography of the CAD model, separately.

The experimental rig is set up for the CAD model based upon the optimal parameters provided in Sect. 4. The experimental prototype and the sensor layout scheme is shown in Figure 8: the static basement and the loading is connected by the displacement-sensor 1 and 2 to measure the absolute displacement of the loading in Y and X directions, respectively, the vibration platform and the static basement is connected by the displacement-sensor 3 and 4 to measure the displacement of the platform in Y and X directions, respectively, and the acceleration-sensor 1 and 2 are mounted on the loading and the vibration platform, respectively, to measure the acceleration in two directions.

Figure 9 shows the results obtained from the sweep experiment over the frequency band between 0.5 and 10 Hz with a constant acceleration amplitude equals to $0.12g$ with the input signal marked black and the response marked red and green for the forward and backward frequency sweeping from and to 0.5 Hz to and from 10 Hz, respectively. Figure 9(a) and (d), 9(b) and (e), and 9(c) and (f) exhibit the displacement signal, the acceleration signal, and the PSD of the acceleration signal in X (Figure 9(a), (b), and (c)) and Y (Figure 9(d), (e), and (f)) directions, respectively.

It is remarkable to find that from the figures, Figure 9(a), (b), (d) and (e), both the displacement and the acceleration responses have been attenuated greatly, the maximum acceleration response is attenuated about 68.0232% and 68.9621% in X and Y direction, respectively, and the initial vibration isolation frequency is about 0.66 and 0.68 Hz in X and Y direction, respectively, the details seen in Figure 9(c) and (f).

The seismic experiment have been finished by input the time domain spectrum of a real earthquake ground motion record plotted in Figure 4 as the control signal to the vibration platform. The vibration directions are along the X and Y axis, respectively, because that the vibration isolation performance of the system in X and Y directions is decoupled, and it is easy to prove that vibration in any direction in the horizontal plane will not destroy the isolator more than that along these two directions.

The responses measured from the experiment under the seismic excitation have been plotted in Figure 10 with the

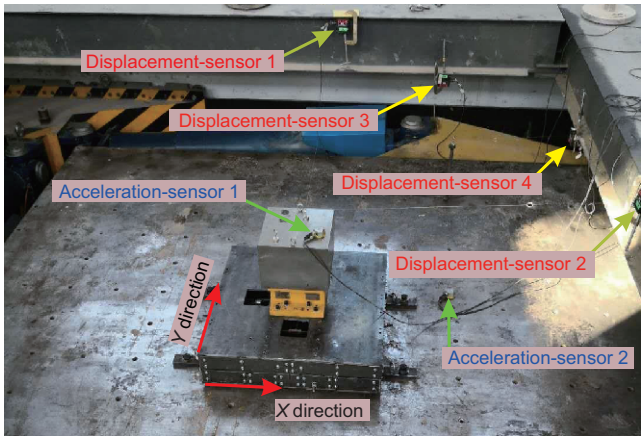

Figure 8 The experimental prototype and the sensor layout scheme.

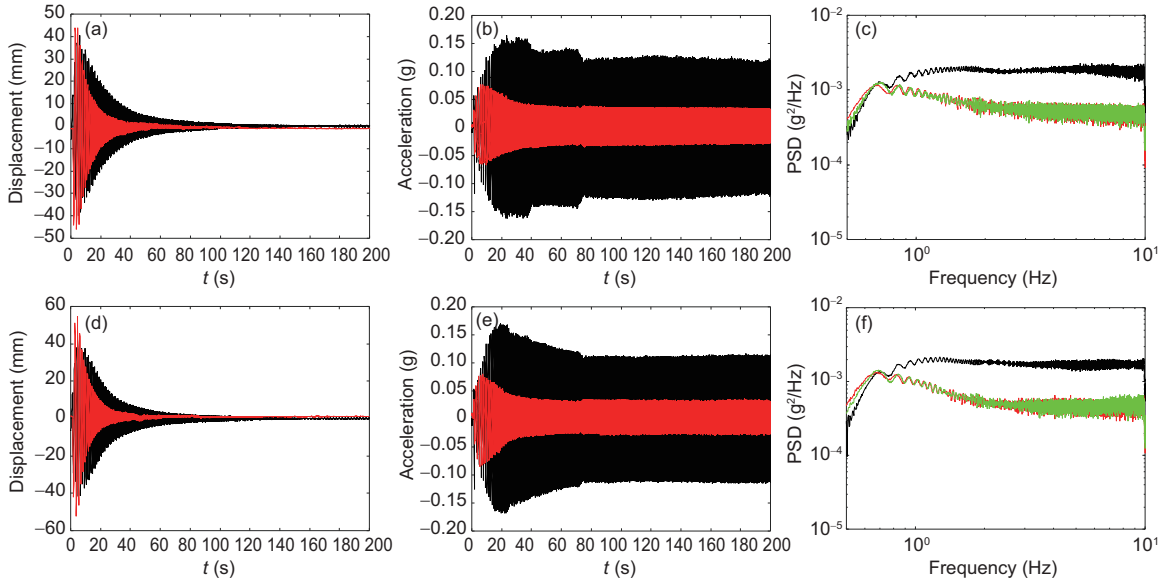

Figure 9 The result of the sweep frequency experiment. (a)–(c) The absolute displacement signal in time domain, the acceleration signal in time domain, and the PSD of the acceleration signal in X direction, respectively; (d)–(f) the absolute displacement signal in time domain, the acceleration signal in time domain, and the PSD of the acceleration signal in Y direction, respectively.

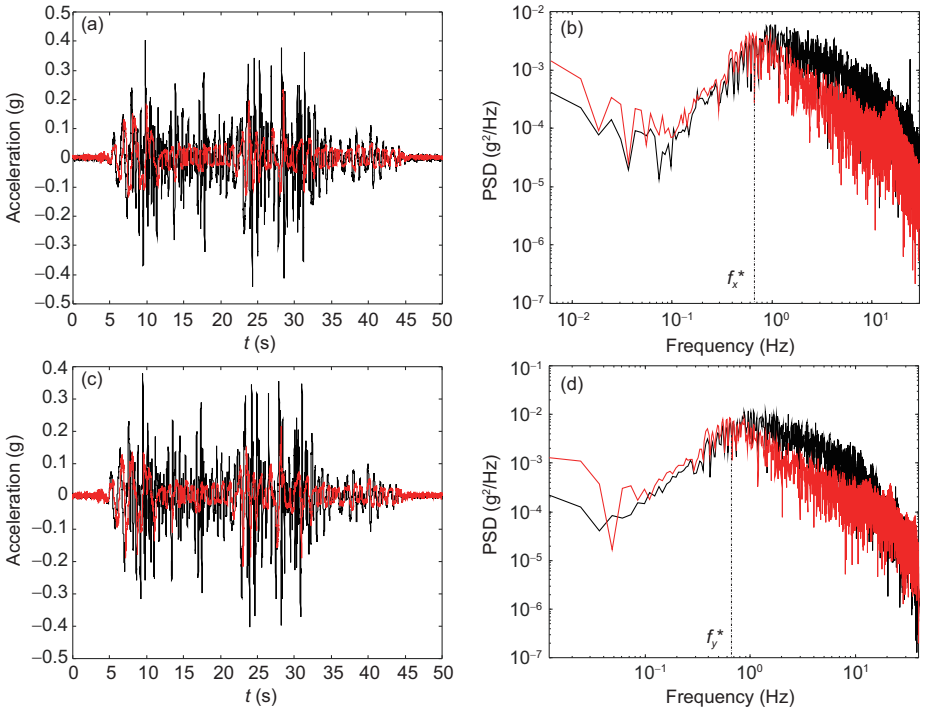

Figure 10 The result of the seismic wave excitation experiment. (a), (b) The acceleration signal along X direction in time and frequency domain, respectively; (c), (d) the acceleration signal along Y direction in time and frequency domain, respectively.

seismic wave acceleration spectrum represented black used in the Sect. 3, and the responses of the loading mass marked red. It is also observed that from Figure 10(a) and (c) the response peak has been attenuated about 41.6783% and 42.516% in X and Y directions, respectively, and the average response has been reduced about 45.3714% and 47.3362% in X and Y directions, respectively. It is also found from Figure 10(b) and (d) that the response in X and Y directions will be attenuated when the frequency is higher than $f_x^* \approx 0.6653$ Hz and $f_y^* \approx 0.6592$ Hz, respectively.

The results presented here show the significant agreement between the experimental investigations and the theoretical analysis, even there exists acceptable errors about 5% and 0.1 Hz for the vibration attenuation ability and the initial vibration isolation frequency, respectively, which might be resulted from the friction between the contact parts of the prototype.

6 Conclusion

In this paper, an archetypal vibration isolator with SQZS in multiple directions based on the SD oscillator has been proposed to protect the structure failure from complex seismic waves horizontally. The SQZS condition has been obtained and the stability has been confirmed by the analysis of the equivalent stiffness characteristics. The analytical transmissibility relationship and the sensitivity of the acceleration and the absolute displacement has been achieved by employing the averaging technique. The results showed that the vibration isolation performance can be effectively improved by the proper choosing of damping ratio. The parameters have also been optimized by the ergodic calculations for both stiffness and damping under the excitation of seismic acceleration record, based upon which the analysis has shown that the resonance of the system can be effectively suppressed about 47.775% and the initial isolation frequency can be decreased to about 0.525 Hz. The 2-DOF experimental rig has been set up and the experimental investigations have been carried out to investigate the aseismic performance of the proposed model by frequency sweeping and seismic wave excitation. The experimental results demonstrated the vibration isolation performance having a good agreement with the theoretical analysis, the maximum error within 5% and 0.1 Hz for the vibration attenuation capacity and the initial vibration isolation frequency, respectively. The results presented herein this paper would lay a foundation for the aseismic engineering to protect the failure of electric power system under the complex excitation of seismic waves.

The first three authors acknowledge the financial support from the National Natural Science Foundation of China (Grant Nos. 11572096, 11732006).

1 Kramer S L. Geotechnical Earthquake Engineering. In: Prentice-Hall International Series in Civil Engineering and Engineering Mechanics. Upper Saddle River: Prentice-Hall, 1996. 653

2 Gregori S D, Christiansen R. Seismic hazard analysis for central-western Argentina. Geodesy GeoDyn, 2018, 9: 25–33
3 Main I. Earthquake hazard analysis: Issues and insights. Surv Geophys, 1992, 13: 297–298
4 Sun Y H, Cheng Y F, Lu Z C, et al. Experimental research on seismic performance of UHV GIS porcelain bushing and composite bushing. High Voltage Eng, 2019, 45: 541–548
5 Liu J, Liu A W, Sun J N, et al. Analysis on characteristics of the hazards of the 2015 Pishan MS 6.5 earthquake in Xinjiang. Earthquake Res China, 2017, 31: 116–124
6 Fukahori Y, Kojima H, Ogino A, et al. Anti-seismic device. US Patent. 4, 899, 323. 1990-2-6
7 Fukahori Y, Kojima H, Ogino A. Anti-seismic bearing. US Patent. 4, 978, 581. 1990-12-18
8 Scozzese F, Dall'Asta A, Tubaldi E. Seismic risk sensitivity of structures equipped with anti-seismic devices with uncertain properties. Struct Saf, 2019, 77: 30–47
9 Al Qablan H, Rababeh S, Katkhuda H, et al. On the use of wooden beams as an anti-seismic device in stone masonry in Qasr el-Bint, Petra, Jordan. J Building Eng, 2019, 21: 82–96
10 Marini A, Belleri A, Preti M, et al. Lightweight extrados restraining elements for the anti-seismic retrofit of single leaf vaults. Eng Struct, 2017, 141: 543–554
11 Guo Z G, Sun W M, Ni T Y, et al. Earthquake damage and anti-seismic behavior analysis of school buildings in Wenchuan earthquake. J Nanjing Univ Tech (Nat Sci Ed), 2009, 1: 010
12 Cheng Y F, Zhu Q J, Lu Z C. Progress and development trend on seismic measures of electric power equipments in transformer substation. Power System Tech, 2008, 32: 84–89
13 Zhu R M, Li D L, Qi L Z, et al. Earthquake disaster analysis and anti-seismic design for substations. Electric Power Construct, 2013, 4: 14–18
14 Xie Q, Zhu R Y, Qu W J. Analysis on seismic failure mechanism of 500 kV high-power transformer during Wenchuan earthquake. Power System Tech, 2011, 35: 221–226
15 Liu R S, Zhang M J, Liu Y, et al. Damage and failure study of sichuan electric power grid in Wenchuan earthquake. J Basic Sci Eng, 2010, 18: 200–211
16 Zhang X H, Wu G Y, Jiang W, et al. Effects of Wenchuan earthquake on Sichuan grid. Modern Electric Power, 2009, 26: 4–9
17 You H B, Zhao F X. M7.0 earthquake in Lushan and damage cause analysis of power facilities. Electric Power Construct, 2013, 34: 100–104
18 Liu R S, Liu J L, Yan D Q, et al. Seismic damage investigation and analysis of electric power system in Lushan MS 7.0 earthquake. J Natural Disasters, 2013, 22: 83–90
19 Huang X T. The Near-field Strong Ground Motion Characteristics of Lushan Earthquake. Dissertation for Dcotoral Degree. Institute of Engineering Mechanics, China Earthquake Administration, 2014
20 Alabuzhev P, Gritchin A. Vibration Protection and Measuring Systems with Quasi-zero Stiffness. New York: Hemisphere Publishing Corporation, 1989
21 Zhang J Z, Li D, Chen M J, et al. An ultra-low frequency parallel connection nonlinear isolator for precision instruments. Key Eng Mater, 2004, 257-258: 231–238
22 Winterflood J, Blair D G, Slagmolen B. High performance vibration isolation using springs in Euler column buckling mode. Phys Lett A, 2002, 300: 122–130
23 Plaut R H, Sidbury J E, Virgin L N. Analysis of buckled and pre-bent fixed-end columns used as vibration isolators. J Sound Vib, 2005, 283: 1216–1228
24 Liu X, Huang X, Hua H. On the characteristics of a quasi-zero stiffness isolator using Euler buckled beam as negative stiffness corrector. J Sound Vib, 2013, 332: 3359–3376
25 Santillan S, Virgin L N, Plaut R H. Equilibria and vibration of a heavy pinched loop. J Sound Vib, 2005, 288: 81–90
26 Virgin L N, Santillan S T, Plaut R H. Vibration isolation using extreme geometric nonlinearity. J Sound Vib, 2008, 315: 721–731
27 Zhou N, Liu K. A tunable high-static-low-dynamic stiffness vibration isolator. J Sound Vib, 2010, 329: 1254–1273
28 Robertson W S, Kidner M R F, Cazzolato B S, et al. Theoretical design parameters for a quasi-zero stiffness magnetic spring for vibration isolation. J Sound Vib, 2009, 326: 88–103
29 Xu D, Yu Q, Zhou J, et al. Theoretical and experimental analyses of a nonlinear magnetic vibration isolator with quasi-zero-stiffness characteristic. J Sound Vib, 2013, 332: 3377–3389
30 Zhou J, Wang X, Xu D, et al. Nonlinear dynamic characteristics of a quasi-zero stiffness vibration isolator with cam-roller-spring mechanisms. J Sound Vib, 2015, 346: 53–69
31 Zhao J X, Yu X, Chai K, et al. Attractor migration control of a vibration isolation system with quasi zero stiffness. J Vib Shock, 2018, 37: 220–224
32 Carrella A, Brennan M J, Waters T P. Optimization of a quasi-zero-stiffness isolator. J Mech Sci Technol, 2007, 21: 946–949
33 Yu J Y. Characteristics analysis and experimental research on quasi-zero-stiffness vibration isolation system based on SD oscillator. Dissertation for dcotoral degree. Shijiazhuang: Shijiazhuang Tiedao University, 2018
34 Cao Q, Wiercigroch M, Pavlovskaia E E, et al. Archetypal oscillator for smooth and discontinuous dynamics. Phys Rev E, 2006, 74: 046218
35 Cao Q, Wiercigroch M, Pavlovskaia E E, et al. Piecewise linear approach to an archetypal oscillator for smooth and discontinuous dynamics. Philos Trans R Soc A-Math Phys Eng Sci, 2008, 366: 635–652
36 Yue X L, Xu W, Wang L. Stochastic bifurcations in the SD (smooth and discontinuous) oscillator under bounded noise excitation. Sci China-Phys Mech Astron, 2013, 56: 1010–1016
37 Yang J, Xiong Y P, Xing J T. Power flow behaviour and dynamic performance of a nonlinear vibration absorber coupled to a nonlinear oscillator. Nonlinear Dyn, 2015, 80: 1063–1079
38 Chen H, Xie J. Harmonic and subharmonic solutions of the SD oscillator. Nonlinear Dyn, 2016, 84: 2477–2486
39 Santhosh B, Padmanabhan C, Narayanan S. Numeric-analytic solutions of the smooth and discontinuous oscillator. Int J Mech Sci, 2014, 84: 102–119
40 Xing J T. Energy Flow Theory of Nonlinear Dynamical Systems with Applications. Springer International Publishing, 2015
41 Cao Q J, Leger A, Wiercigroch M. A Smooth and Discontinuous Oscillator. Springer Tracts in Mechanical Engineering, 2016
42 Hao Z, Cao Q. The isolation characteristics of an archetypal dynamical model with stable-quasi-zero-stiffness. J Sound Vib, 2015, 340: 61–79
43 Carrella A, Brennan M J, Waters T P. Static analysis of a passive vibration isolator with quasi-zero-stiffness characteristic. J Sound Vib, 2007, 301: 678–689
44 Kovacic I, Brennan M J, Waters T P. A study of a nonlinear vibration isolator with a quasi-zero stiffness characteristic. J Sound Vib, 2008, 315: 700–711
45 Sun X, Xu J, Jing X, et al. Beneficial performance of a quasi-zero-stiffness vibration isolator with time-delayed active control. Int J Mech Sci, 2014, 82: 32–40
46 Zhu G N. Anti-seismic and vibration isolation study on a nonlinear system with quasi-zero stiffness. Dissertation for dcotoral degree. Harbin: Harbin Institute of Technology, 2017